Plasmon-triggered living photopolymerization for elaboration of hybrid polymer/metal nanoparticles

Farid Kameche, Wajdi Heni, Siham Telitel, Dandan Ge, Loïc Vidal, Frederic Dumur, Didier Gigmes, Jacques Lalevee, Sylvie Marguet, Ludovic Douillard, et al.

AUTHOR QUERY FORM

ELSEVIER	Journal: MATTOD Article Number: 1614	Please e-mail your responses and any corrections to: E-mail:

Dear Author,

Please check your proof carefully and mark all corrections at the appropriate place in the proof (e.g., by using on-screen annotation in the PDF file) or compile them in a separate list. Note: if you opt to annotate the file with software other than Adobe Reader then please also highlight the appropriate place in the PDF file. To ensure fast publication of your paper please return your corrections within 48 hours.

For correction or revision of any artwork, please consult http://www.elsevier.com/artworkinstructions.

Any queries or remarks that have arisen during the processing of your manuscript are listed below and highlighted by flags in the proof. Click on the `Q' link to go to the location in the proof.

Location in article	Query / Remark: click on the Q link to go Please insert your reply or correction at the corresponding line in the proof
Q1	The author names have been tagged as given names and surnames (surnames are highlighted in teal color). Please confirm if they have been identified correctly.
Q2	Your article is registered as a regular item and is being processed for inclusion in a regular issue of the journal. If this is NOT correct and your article belongs to a Special Issue/Collection please contact r.sanden@elsevier.com immediately prior to returning your corrections.

Please check this box if you have no corrections to make to the PDF file ☐

Thank you for your assistance.

Graphical abstract

Plasmon-triggered living photopolymerization for elaboration of hybrid polymer/metal nanoparticles

pp xxx–xxx

Farid Kameche, Wajdi Heni, Siham Telitel, Dandan Ge, Loïc Vidal,
Fréderic Dumur, Didier Gigmes, Jacques Lalevée, Sylvie Marguet,
Ludovic Douillard, Céline Fiorini-Debuisschert, Renaud Bachelot, Olivier Soppera *

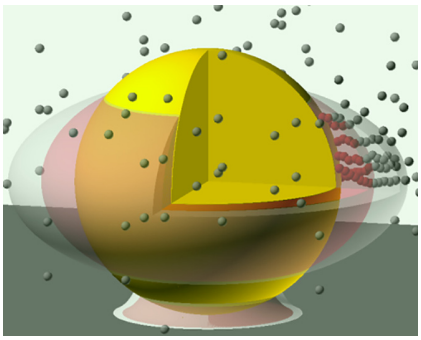

Materials Today • Volume xxx, Number xx • xxxx 2020 RESEARCH

ELSEVIER

Plasmon-triggered living photopolymerization for elaboration of hybrid polymer/metal nanoparticles

Farid Kameche [1], Wajdi Heni [1], Siham Telitel [1], Dandan Ge [2], Loïc Vidal [1], Fréderic Dumur [3], Didier Gigmes [3], Jacques Lalevée [1], Sylvie Marguet [4], Ludovic Douillard [5], Céline Fiorini-Debuisschert [5], Renaud Bachelot [2,6], Olivier Soppera [1,*]

[1] Institut de Science des Matériaux de Mulhouse (IS2M), CNRS UMR 7361, Université de Haute-Alsace, Mulhouse, France
[2] Light, nanomaterials, nanotechnologies (L2n) Laboratory, ICD CNRS, Université de Technologie de Troyes, 10004 Troyes, France
[3] Aix Marseille Univ, CNRS, ICR UMR 7273, Marseille F-13397, France
[4] Université Paris-Saclay, CEA, CNRS, NIMBE, F-91191 Gif-sur-Yvette, France
[5] Université Paris-Saclay, CEA, CNRS, SPEC, F-91191 Gif-sur-Yvette, France
[6] Sino-European School of Technology, Shanghai University, 200444 Shanghai, China

Surface plasmon resonance can be used to manipulate light at the nanoscale. It was used here to trigger photopolymerization of an atom transfer radical polymerization (ATRP) molecular system, leading to a thin polymer shell at the surface of the metal nanostructure. The polymerization can be reactivated from the first polymer shell to covalently graft a second monomer layer with precise control over the thickness at the nanometric scale, depending on the photonic parameters. This route can be applied to different nanoobjects and allows an anisotropic surface modification in agreement with the spatial localization of the enhanced electromagnetic field near the nanostructure. This new route opens the door towards the preparation of multifunctional hybrid metal/polymer nanostructures.

Introduction

Reversible deactivation radical polymerization (RDRP) has proved to be a powerful tool for preparing polymers, with high control over the structure at the molecular scale. Using RDRP, it is possible to precisely control the architecture of polymers and their average molar masses with narrow molecular weight distributions. Several strategies for RDRP have been developed, such as nitroxide mediated polymerization (NMP) [1–3], reversible addition–fragmentation chain transfer polymerization (RAFT) [4,5] or atom transfer radical polymerization (ATRP) [6–11], which can be applied to many different families of monomers. Recently, new approaches have been developed to trigger RDRP reactions by light to achieve photoinduced polymerization [12,13]. Main attainments were reported in review papers [12–16]. In this case, a light source (LED, laser, lamp, etc.) is used to provide the energy to excite the photoactive catalyst to the state necessary to start the polymerization process. Most RDRP techniques have been adapted to photoactivation; examples such as PhotoATRP [6,8,11,17], PhotoNMP (NMP2) [1,18,19], and PhotoRAFT [5] can be found in recent literature. These reactions usually rely on organometallic catalysts or metal ions where the metal can be copper [6,20–22], zirconium [7], ruthenium [23], iron [8,24], cobalt [25], gold [9], manganese [10,26] or iridium [11,27–30]. One of the interests of this photoactivation pathway is linked to the possibility of spatially and temporally controlling the polymerization reaction. The polymerization starts upon irradiation in irradiated areas, stops when irradiation is stopped and can be reactivated to start the cycle many times. In addition, phototriggered RDRP has opened new possibilities in the field of micro- and nanofabrication, using the spatial control of a photoactivated reaction. Several examples have shown

* Corresponding author.
E-mail address: Soppera, O. (olivier.soppera@uha.fr)

 https://doi.org/10.1016/j.mattod.2020.03.023

Please cite this article in press as: F. Kameche et al., Materials Today (2020), https://doi.org/10.1016/j.mattod.2020.03.023

the possibility of restarting the polymerization from a first polymer surface [19,20,28,31–33], leading to the *in situ* synthesis of a copolymer structure on the first polymer surface. For example, Wang et al. [33] demonstrated the grafting of copolymer brushes on silicon. They photopolymerized a first layer of a methylmethacrylate polymer brush on the substrate in the presence of an initiator and a catalyst. Then, using a mask, a second photopolymerization of a hydrophobic fluorinated monomer was triggered onto the previously generated polymer brushes. Using an iridium complex as a photoinitiator catalyst, Telitel et al. [28] polymerized *via* ATRP a photopolymer film on a substrate followed by a local polymerization of a monomer onto the film using direct laser writing. By adding a drop of a monomer and using a light source, the polymerization was easily triggered because of the presence of the iridium complex, which is regenerated through a catalytic cycle.

In both cases, control of the polymer thickness was achieved by tuning the photonic parameters, such as light power or irradiation time, but high-resolution patterning has not yet been explored. One of the fundamental interests of the work presented in this paper is to investigate the possibility of using PhotoRDRP to reach nanoscale resolution.

For this purpose, we used an optical near-field (ONF) photopolymerization approach. ONF is intrinsically a nondiffraction-limited technique and is thus compatible with nanoscale photofabrication. The idea behind ONF is to benefit from the local enhancement of the electromagnetic field in the vicinity of metal nanostructures excited by light. Indeed, upon plasmonic excitation, metal nanostructures exhibit highly confined near-fields close to their surfaces. In this context, the use of a suitable photopolymer in well-controlled conditions opens the way to confine the polymerization to this nanoscale volume under the condition that the diffusion of reactive species is controlled.

The proof of concept was proposed by several teams, including our consortium [34–38]. Using atomic force microscopy (AFM), the photopolymerization of a triacrylate monomer around silver nanoparticles (NPs) was demonstrated. Ueno et al. used gold nanoblocks to trigger photopolymerization between them according to a certain polarization direction [39]. In all those cases, the formed photopolymer had a nanometer volume. One of the practical motivations of this approach is to provide access to a convenient process to produce hybrid polymer–metal nanostructures with original optical properties. From a more fundamental point of view, this configuration is also a unique method for investigating photoinduced polymerization at the nanoscale, which brings information on specific physico-chemical phenomena occurring with extreme confinement [37].

Although the feasibility has been proved, the application of this concept has been limited to only a few photopolymer systems. Coupling ONF photopolymerization and PhotoRDRP opens new perspectives, which motivated us to carry out this work.

We first demonstrate that PhotoATRP can be used in the ONF configuration, leading to nanoscale photopolymerization. Compared to previous works, we have used an iridium complex (namely, $Ir(piq)_2(tmd)$) [28,29,40] that is interesting for its absorbance band, which is extended towards high wavelengths. This condition is important since an overlap between the extinction spectrum of the metal NP and the absorption spectrum of the photopolymer is required.

Due to the high confinement of the photopolymerization observed in this configuration, a new experimental strategy was developed to characterize the polymerization process at the nanoscale: the complete process was conducted on Si_3N_4 membranes of transmission electron microscopy (TEM) grids. This allows the following individual NPs to be characterized after each step of the process with nanoscale resolution. The main advantages over previous studies based on scanning electron microscopy (SEM) and/or AFM are a better resolution and a fast view over a large number of NPs that allows one to carry out a statistical analysis. Moreover, TEM allows a precise characterization of the NPs, such as their crystallinity, their shape, the presence of residual surfactant and the possibility to observe it in 3D thanks to a tomographic mode.

The impact of the main parameters on the efficiency of the photopolymerization is studied to investigate the principal physico-chemical parameters driving the process. Then, we show that the polymerization can be reactivated from the nanoscale first layer. The 3D spatial extent of the polymer is compared to the spatial distribution of the electromagnetic near-field. Moreover, the confinement mechanism is also discussed. Herein, we thus explore the limits of PhotoATRP in terms of resolution thanks to ONF photopolymerization. In addition to the fundamental science, an illustration of the interest of this nanofabrication toolbox for complex metal nanostructures and multichemistry is given in the last part. The objective is to open new opportunities to build complex hybrid metal–polymer nanosystems with tunable compositions in shape and chemistry. One original feature of this NP preparation pathway is the possibility of obtaining anisotropic functionalized NPs with control over the surface chemistry and position of the polymer at the nanoscale.

This process makes it possible to prepare metal/polymer hybrid nanoparticles with a complex polymer structure (multichemical and anisotropic), while remaining relatively simple to implement. It is therefore useful for any application for which such objects are indispensable: for biomedical applications, such nanoparticles are very interesting for synthesizing injectable nanomaterials for the transport and delivery of drugs. Nanosensor applications can be envisaged, where the covalent grafting of the sensitive layer onto the metal structure would be very precise, controlled and facilitated. Applications in nanophotonics in which the grafting of photoactivatable molecules (fluorophores, photochromes...) could be placed very precisely on the metal surface are possible. Also, the grafting of multilayer polymers onto metallic objects allows the preparation of nanoobjects that couple optical and mechanical responses (for thermoresponsive hybrid metasurfaces for example).

Experimental methods

Preparation of the formulation.

The iridium complex is (*bis*(1-phenylisoquinolinato-N,C2′)iridium(2,2,6,6-tetramethyl-3,5-heptanedionate), denoted as Ir

Please cite this article in press as: F. Kameche et al., Materials Today (2020), https://doi.org/10.1016/j.mattod.2020.03.023

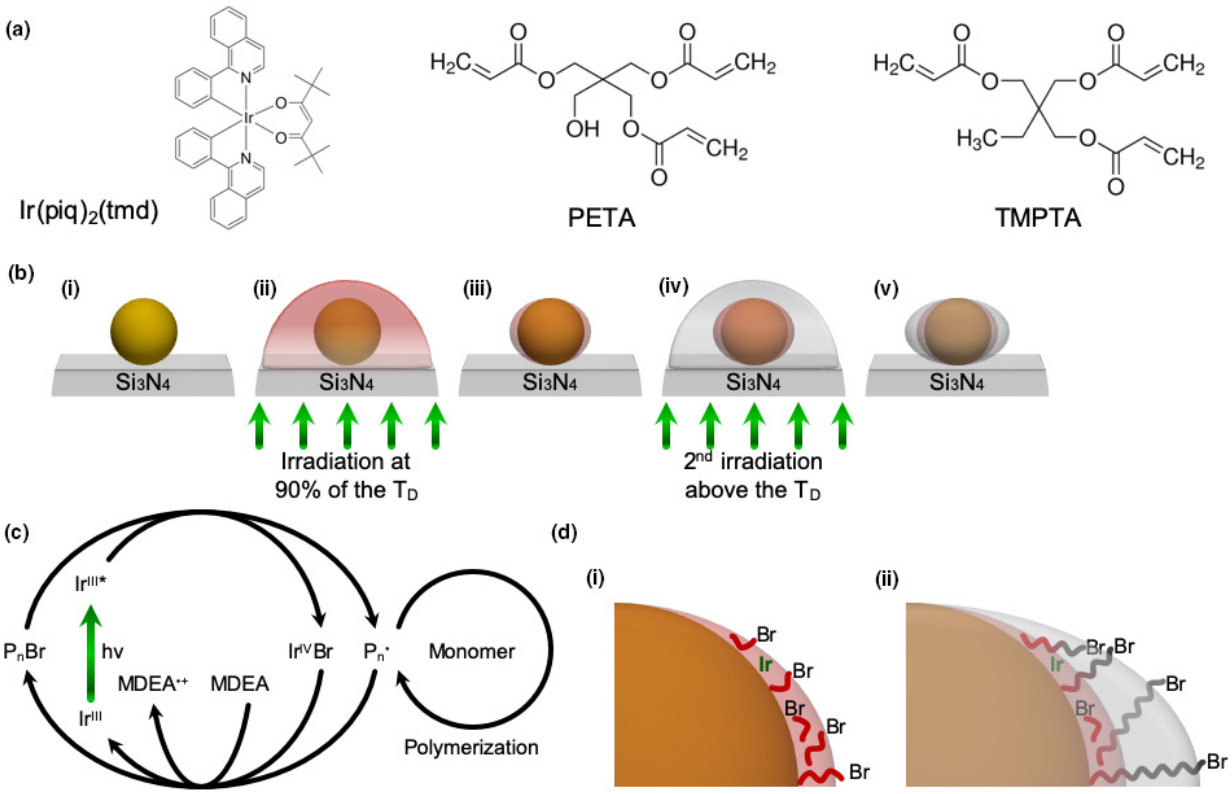

FIGURE 1

(a) Chemical structure of the the Ir(piq)$_2$(tmd) complex, PETA and TMPTA acrylate monomers. (b) Schematic of the hybrid nanoparticle preparation process by PhotoATRP. (i): 43 nm-diameter gold NPs are deposited onto the TEM grid. (ii): The TEM grid is covered with a drop of the photopolymerizable formulation, and the irradiation is performed at 90% of the threshold dose. (iii): The sample is developed with ethanol and characterized by TEM. (iv): A second irradiation is performed in the presence of a second monomer, without a photoinitiator. (v): The sample is developed, revealing the second polymer layer covalently bounded to the first layer. (c) Photoinduced molecular mechanism of PhotoATRP. (d) Schematic of the nanoparticle surface after (i) the first photopolymerization and (ii) the second photopolymerization.

(piq)$_2$(tmd) (Fig. 1a). Its synthesis is described in the paper of Tian et al. [40]. The photopolymerizable formulation was prepared by mixing Ir(piq)$_2$(tmd), 2-bromoacetophenone (denoted as PBr), and *N*-methyldiethanolamine (MDEA) in pentaerythritol triacrylate (PETA), without the use of a solvent. These products were obtained from Sigma-Aldrich and were used as received. The composition was set to 1 wt. % Ir(piq)$_2$(tmd), 3 wt. % PBr and 4 wt. % MDEA. Trimethylolpropane triacrylate (TMPTA) and 2,2,3,4,4,4-hexafluorobutyl acrylate (HFBA) were purchased from Sigma-Aldrich. The formulas of acrylate monomers can be found in Fig. 1a. Other compounds are depicted in Fig. S1 in the supporting information (SI).

Spherical (43 nm diameter) and cubic (57 nm edge) gold NPs were prepared by colloidal chemistry using cetyltrimethylammonium bromide (CTAB) as the capping agent [41–44]. The cubes were obtained, in a first step, according to an already published protocol [41,42]. They were converted to highly spherical nanospheres in a second step by chemical etching in the presence of $HAuCl_4$ and CTAB. The oxidation of Au nanocrystals with Au (III)–CTAB complexes was indeed shown to occur preferentially at surface sites with high curvatures [43,44]. The surfactant was removed from the surfaces of the NP by centrifugation in an aqueous solution and UV-ozone treatment after drop deposition onto the substrate. TEM was used to characterize the NP size distribution and confirm the elimination of the surfactant (Fig. S2).

Characterization of samples

TEM characterization was conducted on 2 microscopes. A PHILIPS CM200 TEM was used to characterize NPs after each step of the near-field photopolymerization process. An ARM200F JEOL High-Resolution transmission electron microscope equipped with a double tilt sample holder (tilting angle tunable from +60° to −60°) was used to perform tilt experiments. In all cases, silicon TEM grids with two rectangular slits (1500 μm × 100 μm) covered on one face with a 50 nm-thick Si_3N_4 membrane were used (TEDPELLA). ImageJ v.1.8 software was used to adjust the brightness and contrast levels of the TEM images and evaluate the thickness of the polymer shell from the TEM images.

Simulations

The experiment is complemented by numerical simulations based on the boundary element method (BEM) *via* its implementation in the *multiple nanoparticles BEM* MNPBEM toolbox [45,46]. The BEM approach provides solutions of Maxwell's equations in the case of arbitrarily shaped dielectric interfaces. The solutions are expressed in terms of surface charges and currents,

Please cite this article in press as: F. Kameche et al., Materials Today (2020), https://doi.org/10.1016/j.mattod.2020.03.023

so that only surfaces between the different materials have to be discretized providing fast simulations. For more details, see [47,48]. A Au sphere 43 nm in diameter is modeled on an infinite Si_3N_4 substrate. The distance between the Au NP and the substrate is fixed at 1 nm. The NP is covered by a monomer formulation with a refractive index $n = 1.48$. The refractive index of Au is taken from Johnson and Christy [49], that of the Si_3N_4 substrate is fixed $\mathbf{atn}_{\mathbf{Si_3N_4}} = 2.056$ [50]. Illumination is carried out from the wide band gap semiconductor substrate side under normal incidence with a circular polarized 532 nm light source. Simulations carried out in quasistatic and retarded field approximations give similar results. Maps of the squared modulus of the optical near electric field $|E_{nf}|^2$ around one Au NP are determined. Note that incident field amplitude is normalized to unity within the substrate. Equivalent numerical simulations have been conducted on 57 nm edge Au cubes. In addition to field maps, extinction spectra have also been calculated.

Optical near-field photopolymerization process

Before the deposition of NPs onto the TEM grids, the TEM grids were functionalized by a self-assembled APTS monolayer ((3-Aminopropyl)triethoxysilane from Sigma-Aldrich) to promote the anchoring of the NPs onto the substrate surface. UV-ozone treatment was then used to remove the surfactant at the surface of the NP. The TEM grid with gold NPs deposited on its surface (Fig. 1b-i) was put in the pathway of a frequency-doubled Nd-YAG laser (532 nm, 6 W, VERDI model from Coherent). The details of the optical setup are given in Fig. S3. The setup was designed to generate a collimated illumination, with a homogeneous power density over the area of interest (typ. a few mW/cm^2 on 1 cm^2) and with circular polarization. Once properly placed, a drop of the formulation (4 μL) was deposited onto the TEM grid. The laser beam irradiated the photopolymer through the Si_3N_4 substrate (wide band gap semiconductor) so that there was no attenuation of the laser beam by the photopolymer on the plane of the NPs. The polymerization threshold time (t_T) was determined in a separate experiment. This corresponds to the minimum time needed to start the polymerization at the substrate surface for a given light power density [37]. To determine it experimentally, the liquid photopolymer was deposited onto the TEM membrane (without NPs), irradiated, rinsed in ethanol and observed by optical microscopy. When polymer parts are observed on the TEM grid, the threshold time of polymerization is reached. In the presence of the NPs, the sample was typically irradiated at 90% t_T (Fig. 1b-ii). Under such conditions, far-field photopolymerization is avoided, while plasmonic intensity enhancement in the near-field of NPs (typically by a factor of 28, see below) provokes the start of photopolymerization in this nanovolume. After irradiation, the sample was rinsed by immersion for 10 min in an ethanol bath. Then, the sample was dried in air and characterized by TEM (Fig. 1b-iii). The entire process was carried out under inactinic red light to avoid any degradation of the photocatalyst. In a second step, repolymerization from the surface was tested by placing the grid in the same optical setup. It was irradiated after being covered by a monomer (generally TMPTA). For this step, no photoinitiator was added to the monomer (Fig. 1b-iv). The development step was performed in exactly the same way as for the first step, and the NPs studied after the first exposure were characterized once again (Fig. 1b-v). Several examples are given in the SI to show that the same NPs could be found after different steps of the process.

Results and discussion

Photopolymerizable formulation

The molecular process for light-induced controlled photopolymerization can be described as proposed by Hawker et al. (Fig. 1c) [31]. At the molecular scale, the scheme is basically an oxidative catalytic cycle involving the iridium complex. After light absorption, the complex in its excited state reduces an alkyl bromide to generate the alkyl radical that initiates the polymerization of the acrylate monomers. The oxidizing state ($Ir^{IV}Br$) can then react with a propagating radical, which regenerates the initial Ir^{III} in its ground state and a dormant polymer chain with a bromo end group. Photopolymerization triggered by the $Ir(piq)_2(tmd)$ complex was confirmed in previous studies [27–29]. The behavior of Ir complexes in oxidative catalytic cycles has been established by Telitel et al. [51] It has also been shown that additional amines can be used as reductive agents to regenerate Ir^{III} from Ir^{IV}, significantly improving the polymerization kinetics. Therefore, the three-component Ir^{III}/PBr/amine system combines fast initiation and polymerization rates with good control of the chain end. Due to this livingness property, we expect that the first polymer shell on gold NPs contains reactivable Ir complexes (Fig. 1d-i) that can start a second photopolymerization (Fig. 1d-ii). The presence of metal could be problematic for certain applications, especially in biology. However, the presence of Ir complex in the final material does not appear as central as the concentration of the Ir complex is only 1 wt %, which means that the amount of Ir in the nano-sized polymer lobes is very low. Additionally the second polymer layer grafted onto the first acts as a barrier masking the Ir complexes from the external environment. Moreover, it is likely that some of the Ir complexes are removed during the development step by immersion of the sample in ethanol. This removal is more likely when the thickness of the polymer is very small.

Photopolymerization initiated by the Ir complex in the far-field configuration

The photopolymerization at 532 nm in the far-field configuration (e.g., via irradiation by a propagative plane wave in a thin film, without the presence of the NP) was first checked to confirm the negative tone behavior of the photopolymer. In particular, we characterized the polymerization threshold energy for several light power densities. This value is not only important from a practical point of view to determine the exposure conditions but also brings additional information on the photochemical phenomena involved in the material. The t_T irradiation time was determined for different power densities (0.8 mW/cm^2, 2.5 mW/cm^2, 4.8 mW/cm^2, 7.2 mW/cm^2 and 9.9 mW/cm^2) and plotted in Fig. 2a (black segments). For each power density, the times above and below the threshold dose are represented by blue and red crosses, respectively. These values give good precision regarding the t_T values. As expected, the higher the power density is, the lower the threshold time. The threshold energy (E_T) was then calculated by multiplying t_T by the power density

Please cite this article in press as: F. Kameche et al., Materials Today (2020), https://doi.org/10.1016/j.mattod.2020.03.023

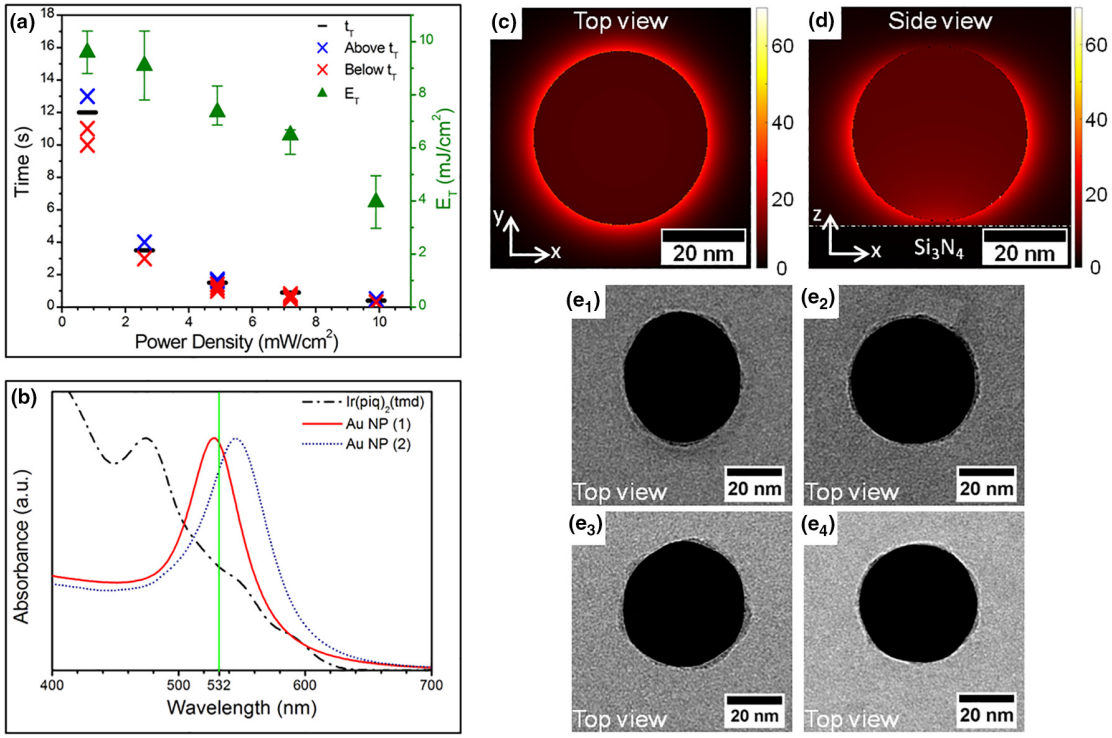

FIGURE 2

(a) Threshold time (t_T, black segments) and threshold energy density (E_T, green triangles) determined for different power densities. The blue and red crosses represent the doses for which the photopolymerizations occur or not, respectively, at the considered power density. (b) UV–Visible extinction spectra of the photopolymerizable formulation, the gold NPs dispersed in water (Au NP (1)) and the Au NPs deposited on the Si_3N_4 substrate and covered by the photopolymer (simulated BEM extinction spectrum – Au NP (2)). (c and d) Calculated distribution of the square modulus of the optical near electric field enhancement $|E_{nf}/E_{incident}|^2$ around one Au NP evaluated by BEM with irradiation at 532 nm (circularly polarized light propagating along the z direction). (c) top and (d) side views, respectively. Incident field amplitude is normalized to unity within the substrate. (e) TEM images of NPs after a first irradiation at 90% of the threshold dose for a density power of (i) 2.5 mW/cm^2, (ii) 4.8 mW/cm^2, (iii) 7.2 mW/cm^2 and (iv) 9.9 mW/cm^2.

and plotted on the same figure (green triangles). Interestingly, the threshold energy for this system decreases when the power density increases. This effect is significant within the narrow range of laser power used, which means that this system is sensitive to a side reaction. This behavior is characteristic of a photopolymerizable formulation sensitive to oxygen quenching. Indeed, for this system, when the power is decreased, the continuous replenishment of oxygen by diffusion from the nonirradiated area and surrounding area increasingly affects the polymerization. This behavior was frequently observed in free radical polymerization [52,53]. Here, it is more pronounced due to the relatively low photoreactivity of the initiating system. However, the polymerization is achievable in the entire range of tested powers.

Optical near-field photopolymerization

The objective of this section is to demonstrate that this photopolymer is compatible with near-field photopolymerization. Fig. 2b shows the experimental extinction spectrum of the gold NPs in a solution (water $n = 1.33$) and the corresponding calculated spectrum of particles with the same size (43 nm) deposited on a Si_3N_4 substrate and surrounded by PETA (dielectric medium with a refractive index equal to 1.48). The extinction spectrum of the photoinitiating system, given by the iridium complex, is also plotted. It can be observed that there is an overlap of the NPs and the iridium complex spectra at 532 nm (emission wavelength of the laser).

The enhancement and spatial extend distribution of the optical near field around one Au NP are determined from BEM simulations. In more details, maps of the squared modulus of the optical near electric field enhancement $|E_{nf}/E_{incident}|^2$ around one Au NP are determined. Incident field amplitude is normalized to unity within the substrate. Two views are considered, an equatorial top view (Fig. 2c) and a polar side view (Fig. 2d). In the equatorial plane (xy) of the NP, the electromagnetic field shows a circular symmetry in agreement with the circular character of the light excitation. At a distance $r = R + 0.5$ nm where $2R = 43$ nm, the square of the enhancement factor EF amounts to 28.3 (e.g. EF = 5.3). Field map in the polar plane (xz) exhibits maxima close to the equatorial plane of the NP and minima along its polar axis. Field enhancement is minimal (EF = 2.8) at the top of the particle. The presence of a high refractive index substrate (Si_3N_4) results in an additional field enhancement below the NP (asymmetric distribution). Within these near-field volumes with enhanced optical intensities, an acceleration of the polymerization kinetics is expected, and thus, gelification should be reached at lower doses. A dose close to the threshold (90%) was chosen in the following near-field photopolymerization experiments by adjusting the irradiation time according to the light power used.

Please cite this article in press as: F. Kameche et al., Materials Today (2020), https://doi.org/10.1016/j.mattod.2020.03.023

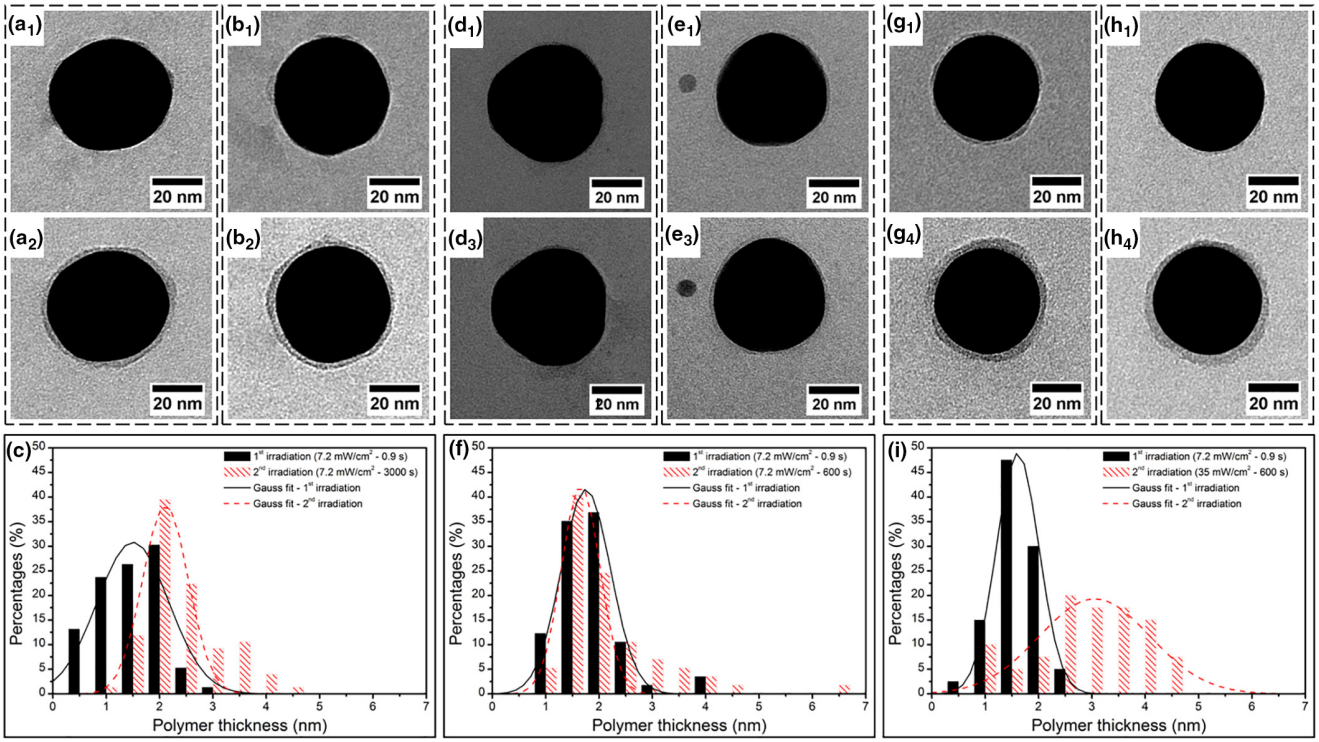

FIGURE 3

(a–b, d–e, g–h) TEM images of two 43 nm gold NPs after (i) the first irradiation at 7.2 mW/cm^2 and at 90% of the threshold dose (irradiation time: 0.9 s) and after the second irradiation at (ii) 7.2 mW/cm^2 for 3000 s, (iii) 7.2 mW/cm^2 for 600 s and (iv) 35 mW/cm^2 for 600 s. (c, f, i) Histogram and Gaussian fit of the photopolymer thickness distribution after (c) irradiation (i) and (ii) (statistics realized on 85 NPs), (f) irradiation (i) and (iii) (statistics realized on 63 NPs) and (i) irradiation (i) and (iv) (statistics realized on 40 NPs). The diameters of the NPs with ($\bar{A}_{NP}$) and without the photopolymer ($\bar{A}_N$) were measured. Afterwards, the thicknesses were calculated by subtracting $\bar{A}_N$ from $\bar{A}_{NP}$ and dividing the result by two.

The effect of power density on the polymerized volume during the first irradiation was studied to define the most suitable condition for near-field photopolymerization (Fig. 2e). Indeed, the intensity of the laser is known to be an important parameter for controlling the shell thickness [37]. Powers were chosen according to Fig. 2a. For each power density, irradiation of the gold NPs with the photopolymerizable formulation at 90% of the threshold dose was performed, and samples were characterized by TEM (Fig. 2ei–eiv). These images are typical images shown in Figs. S4–S6. In each case, the images reveal a thin shell of polymer surrounding the NPs. It turns out that the impact of the power density on the polymer shell thickness is weak. The limited polymer thickness is in agreement with the low photoreactivity of the system, the high sensitivity to the inhibitor, the limited number of photoinitiator molecules in the near-field volume (*ca.* 80 molecules) and the high confinement of the electromagnetic field around the NPs. In the TEM images (top view), the repartition of the polymer follows the expected circular intensity distribution around the equator of the particle, in agreement with the numerical simulations (Fig. 2c).

Considering the very low thickness of the polymer layer, control experiments were conducted to exclude any misinterpretation of these results. In the first control experiment, we verified that the polymer shell is indeed related to the polymer and not to the monomer adsorbed at the surface of the NP, without polymerization. To do so, a drop of the formulation was deposited onto a TEM grid with gold NPs and was not irradiated. The sample was developed in the same way as described above in the experimental part. TEM images were taken before and after the drop deposition and revealed that no formulation remained on the surface of the NPs (see Fig. S2B in the SI). This experiment validates the development process. We also excluded, in our experimental conditions, a direct polymerization of the acrylic monomer as described by Wang et al. [54,55]. In their study, the authors explained that the polymerization on the NP surface is triggered by the ejection of hot electrons, without the need of a photoinitiator. In this case, the control experiment consisted of covering the NP with the raw monomer (without the photoinitiating system) and carrying the irradiation under the conditions described before. The TEM analysis after irradiation did not show any polymer at the surface of the NP, which is consistent with a photoinduced polymerization process following the pathway described in Fig. 1c. In our model, the NP contribution enables modification of the spatial distribution of the electromagnetic near-field, accelerating the photopolymerization in the near-field region.

Repolymerization from the polymer surface

The main objective of this work is to demonstrate the living character of the polymer chains grafted in the first step, *i.e.*, that these chains can be reactivated by irradiation, without an initiator, at the same wavelength to covalently attach another polymer chain

Please cite this article in press as: F. Kameche et al., Materials Today (2020), https://doi.org/10.1016/j.mattod.2020.03.023

at the surface. Here, the power density for the first irradiation was chosen to be 7.2 mW/cm^2. The corresponding irradiation time to reach 90% of the threshold dose is 0.9 s. After the first step described above, different areas on the sample were characterized by TEM, and representative NPs are shown in Fig. 3ai and bi. A thin polymer shell is visible around the NPs, which indicates that photopolymerization was triggered, confirming the results shown in Fig. 2c.

To start the second polymerization, the NPs were covered with pure TMPTA monomer and irradiated with the same configuration, with the same power density as for the first step. The irradiation time was set to 3000 s. For this step, a long irradiation time can be used without far-field polymerization since there is no photoinitiating system in the TMPTA monomer. After irradiation, the sample was rinsed by immersion in ethanol, under conditions identical to those used after the first irradiation. Samples were then characterized by TEM. TEM imaging was carried out on the same NPs that can be found on the TEM grid after each step (Fig. 3aii–bii; see Fig. S7 for TEM images at lower magnifications).

Images aii and bii in Fig. 3 clearly show an increase in the polymerized shell thickness. Fig. 3c presents the statistical analysis of the thickness of the polymer layer around the NPs determined by TEM. Since the thickness is not always homogeneous around the NP, we evaluated the mean thickness as follows: the diameters of the NPs with and without the photopolymer were measured for 85 NPs to evaluate the polymer thickness after the different steps. It appeared that the mean NP shell thicknesses resulting from the first and the second irradiation were 1.24 nm ± 0.55 nm and 2.16 nm ± 0.70 nm, respectively. The increase in thickness after the second irradiation is confirmed by the histogram, where a global shift to higher thicknesses is observed.

To verify that the increase in the polymer layer was indeed induced by laser irradiation, the following control experiment was conducted: after the first step, a drop of TMPTA was deposited onto the sample, and development was done without any irradiation using our standard procedure (Fig. S8). The characterization of the control sample by TEM did not reveal any change in the polymer thickness, demonstrating that the increase in the diameter of the hybrid NP does not result from the adsorption of a thin monomer layer.

Effect of the irradiation conditions on the second polymerization

In the previous experiment, the same power density as for the first polymerization was used, and repolymerization is shown after 3000 s of irradiation. Higher energy is thus required for a second photopolymerization, which we confirmed by using different conditions, as shown in Fig. 3d–i. Previous works on repolymerization at micro- or millimeter scales indeed showed a direct dependence of the polymer layer on the photonic parameters (power density and time) [19,28]. For completeness, additional samples were prepared by performing the first irradiation at 7.2 mW/cm^2 at 90% of the threshold dose and by changing the photonic parameters of the second irradiation.

As observed in the former experiment, a thin polymer shell was observed after the first irradiation (Fig. 3di–ei). In Fig. 3dii–eiii, the second irradiation time was 600 s, and the power density was maintained at 7.2 mW/cm^2. For the second irradiation, there is no clear evidence of a second polymerization. The histogram shown in Fig. 3f confirms this trend for a large number of NPs (63 NPs). We investigated whether the second irradiation efficiency can be improved with higher laser power. In another experiment, the second irradiation was carried out for 600 s with a power density of 35 mW/cm^2, *i.e.*, the total energy was the same as that in the first experiment (cf. Fig. 3aii and bii) but with a higher power density. TEM images of the gold NPs are shown after the first irradiation (Fig. 3gi and hi) and the second irradiation (Fig. 3giv and hiv; see supporting information, Fig. S9). As depicted in the polymer thickness histogram shown in Fig. 3i, these irradiation conditions significantly favor the growth of the second polymer layer since a clear increase in the polymer thickness can be observed. For a given energy, a higher power density favors the growth of the second polymer layer. We conclude from this set of experiments that although the first irradiation is not very efficient, with suitable irradiation conditions, most of the NPs can be functionalized with a polymer shell (at least 90%). We show in these experiments that this thin layer contains enough reactivable species to restart the photopolymerization. In particular, the photosensitive compounds are not washed out during the development steps, and despite the loss of mobility expected in the polymer matrix compared to the photopolymerizable solution in the first step, they are accessible to the second monomer and can still be activated when embedded in the polymer layer.

Moreover, despite the low reactivity of the nanohybrid system during the second irradiation, we demonstrate that the polymerization can be started again as long as the energy delivered is high enough. A low yield can be explained by the inhibition quenching of radical species in the presence of oxygen in the surrounding medium. The impact of the power confirms this assumption since higher power provides a higher rate of radical production and a more efficient competitive pathway against oxygen inhibition. Quenching of the excited states of the iridium complex by the metal nanostructure could also be involved, as it is well known that non-radiative de-excitation occurs in the vicinity of metal NPs [56]. Although this effect may be present, it does not completely inhibit the polymerization in both steps.

3D repartition of the photopolymer

The question of the spatial distribution of the photopolymer around the NPs has been scarcely discussed in previous studies dealing with ONF photopolymerization. The discussion has been indeed limited to observation in 2D due to the limits of the employed imaging techniques (AFM and SEM).

Here, we propose using the tomographic mode of TEM to investigate the spatial distribution of the polymer layer around the NPs. Indeed, the transmission electron microscope used in this study is equipped with a rotation sample holder that makes it possible to record images of the NPs with tilt angles ranging from +60° to −60°.

As shown in the simulations (Fig. 2c and d), the field distribution is not spatially homogeneous around the NP. In the circular polarization and normal irradiation configuration, the near-field enhancement is indeed higher (i) at the equator of the NP and (ii)

Please cite this article in press as: F. Kameche et al., Materials Today (2020), https://doi.org/10.1016/j.mattod.2020.03.023

in the interstice between the NP and the substrate. Case (i) is related to the boundary condition of the field component perpendicular to the metal/dielectric interface: this component is not continuous through the interface and leads to an important polarization charge density at the metal surface. Since the incident field is an in-plane field, this perpendicular component, and the resulting charge density, is maximum along the equator and decreases at locations closer to the poles along the vertical direction. Field enhancement in case (ii) is due to the high refractive index of the substrate (Si_3N_4 membrane) used in these experiments. On the other hand, the near-field is almost null at the other pole of the particle. Based on this last analysis, a representation of a hybrid NP was considered (Fig. 4a), and a tilt experiment was performed to validate it.

After the second polymerization (under the same conditions described in Fig. 3giv and hiv), hybrid NPs were observed along several angles. TEM images for one NP are shown in Fig. 4bi–hi. To acquire an easier view of the results obtained from this experiment, the polymer sections are highlighted in blue (Fig. 4bii–hii). Below, for every angle, a representation of the hybrid NP is shown in Fig. 4biii–hiii and compared to the TEM images. The observation normal to the substrate plane (0°) shows the typical polymer layer around the NP (Fig. 4b). From this image, it is deduced that the polymer shell is present at the equator of the NP, but the electron absorption cross section of the metal being much higher than that of the polymer, it is not possible to confirm the presence of the polymer in other areas of the NP. When the particle is tilted, it is observed that the polymer thickness decreases on one side (top left in Fig. 4ci–hi). The polymer layer disappears after a tilt angle of 30°. The 3D representation in Fig. 4a confirms the absence of polymer at the top (Fig. 4eiii, north pole). On the opposite side (bottom right), the polymer is still visible at 30°, which means that there is polymer below the particle. However, the polymer layer thickness decreases, indicating that the quantity of the polymer below the NP is less than at the equator. These results confirm that the polymer is not distributed homogeneously around the particle but follows the spatial distribution of the calculated electromagnetic field in 3D. From this observation, several conclusions can be made. We first confirm the photochemical nature of the polymerization. Indeed, thermal polymerization would result in a loss of spatial control, leading to a homogeneous polymer layer all over the NP. The second polymerization preserves the spatial distribution, which means that the spatial extent of the repolymerization is well controlled at the nanoscale. Remarkably, this result was obtained despite a small volume corresponding to a very limited number of photoinitiator molecules. Considering a homogeneous distribution of the photoinitiator within the photopolymer, we can indeed estimate an average concentration of one molecule of $Ir(piq)_2(tmd)$ per 100 nm^3, which corresponds roughly to 80 Ir complex molecules in a 2 nm-thick polymer shell. As a consequence, this basic calculation illustrates the small number of reactivable functions within the polymer shell. However, we prove that polymerization can be reactivated, and this is also consistent with the relatively high irradiation conditions needed to obtain a significant repolymerization.

Effect of the shape of NPs on near-field photopolymerization

PhotoATRP can be applied to several nanoobject topologies different from the sphere. In practice, we used dimers, trimers and nanocubes and demonstrated that the ONF photopolymerization principle also applies to these objects. It should be stressed that such nanostructures permit a spatial symmetry breaking of the problem: despite the circular incident polarization, local field enhancement presenting azimuthal anisotropy can be achieved.

PhotoATRP was first applied to dimers. The results are shown in Fig. 5a. In the case of dimers, we expect a maximum enhanced field in the gap between both NPs [57]. Fig. 5ai shows the polymer repartition around the dimer after the first polymerization. Polymer can be distinguished all around the dimer, with a thicker layer at the gap position, as expected. The increase in the polymer shell layer is the most important in the gap, in agreement with a higher field intensity in this region (Fig. 5aii). These observations confirm the photoinduced character of the repolymerization step.

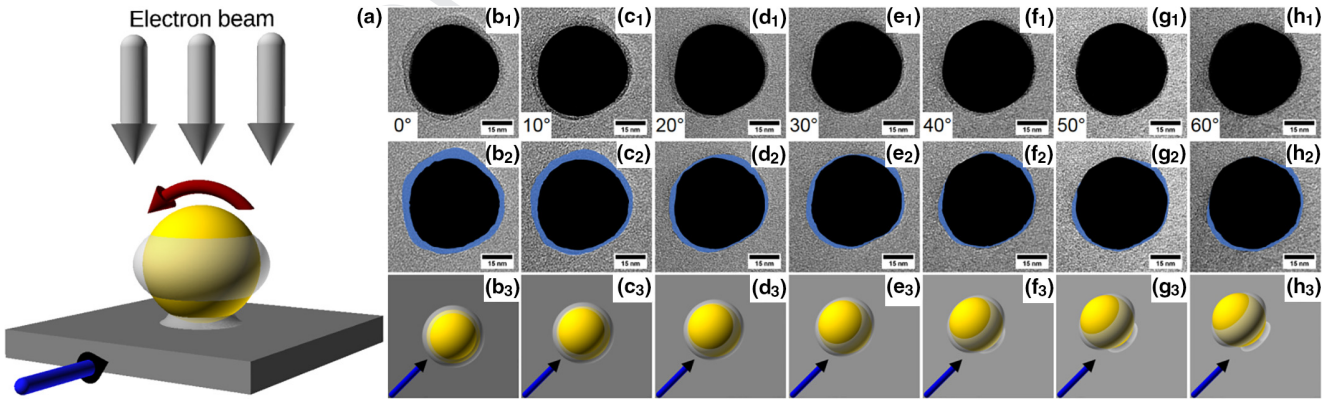

FIGURE 4

(a) Schematic representation of an NP with the second photopolymer shell; the blue arrow represents the rotation axis, and the red arrow indicates the tilt direction: (i) TEM images of the same gold NP (two irradiations under standard conditions) after tilting by (b) 0°, (c) 10°, (d) 20°, (e) 30°, (f) 40°, (g) 50° and (h) 60°. The scale bar represents a length of 15 nm. (ii) TEM images, with the polymer highlighted in blue. (iii) Schematic representation of the tilted NP for the corresponding tilt angle.

Please cite this article in press as: F. Kameche et al., Materials Today (2020), https://doi.org/10.1016/j.mattod.2020.03.023

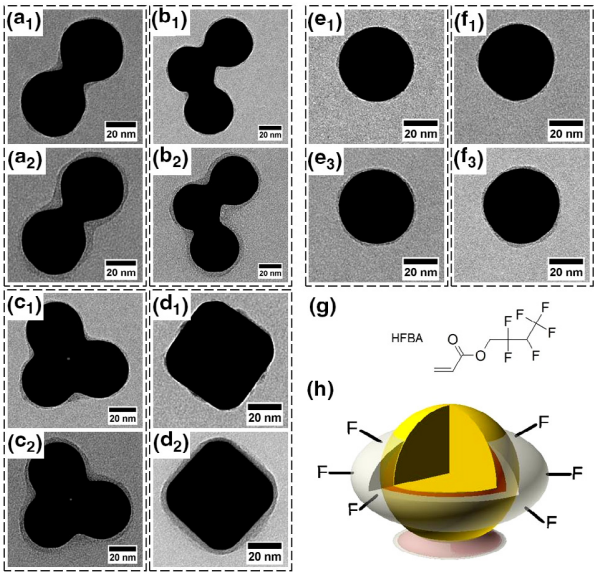

FIGURE 5

TEM images of (a) a dimer and (b and c) trimers of 43 nm gold nanospheres. TEM images of a (d) 57 nm-edge gold nanocube. (e and f) TEM images of 43 nm gold nanospheres. The images were obtained after (i) the first irradiation at 7.2 mW/cm^2 and after the second irradiation, with a circular polarization at 35 mW/cm^2 for 600 s with (ii) TMPTA or (iii) a fluorinated monomer HFBA. (g) Chemical structure of the HFBA fluorinated acrylate monomer. (h) Representation of the double shell system after irradiation under condition (i) and then condition (iii).

The same trend was observed with trimers (Fig. 5b and c). In this case, as expected, the high-field regions are located at the contact positions of the metal NPs. Concerning a closed trimer structure (Fig. 5c), it remains difficult to conclude from the single TEM image regarding the presence or absence of polymer at the center of the trimer, but polymer is very present at the periphery of the object assembly, although the polymer thickness turns out to be clearly larger in regions close to the gaps.

Gold nanocubes with a 57 nm edge length were synthesized according to the procedure described in the literature [41,42] and used here. This size was chosen to obtain a nanocube plasmon resonance that fits with the laser wavelength. A near-field photopolymerization was performed on gold nanocubes deposited onto TEM grids via the same protocol as previously used (Fig. 1b) and under the same conditions as those employed in Fig. 3g and h. Herein (Fig. 5d), the polymer can be grafted onto the lateral sides of the nanocube. The second polymerization was proved to be effective, leading to a relatively thicker shell (Fig. 5dii; see Fig. S10). TEM in tomographic mode (Fig. S11) allowed further investigation of the 3D repartition of the polymer on the cube surface. We demonstrate that there is no polymer on top of the cube, meaning that it is possible to functionalize only the lateral sides of the cube, which is a unique feature of this process.

Tuning the surface chemistry through the choice of the second monomer

Finally, we would like to show the great versatility of the process for tuning the surface chemistry of metal nanoobjects. Indeed, so far, the two polymerizations were performed with two different monomers but with similar structures and properties. Therefore, the second polymerization allowed for the modification of the thickness of the locally grafted polymer but with similar chemical properties. This is interesting, as it demonstrates that the extension was confined to the enhanced field area. Here, we show that other acrylate monomers with very different properties can be used.

HFBA monomer was employed as a substitute for TMPTA in the second polymerization. The objective here is to show that our process can be used to graft a hydrophobic monomer at the surface of the NP and thus change its surface property. Indeed, the contact angles with water of polymer films prepared with PETA, TMPTA or HFBA are quite different (Fig. S12). For the polymer prepared with PETA or TMPTA, the contact angle was found to be close to 55°, but it drastically increased to 106° when it was prepared with HFBA.

The objective here is to show that HFBA can be grafted in the second step. TEM images of NPs after the first irradiation at 7.2 mW/cm^2 at 90% of the threshold dose are shown in Fig. 5ei and fi (see Fig. S13 for more examples of the NPs studied). A thin polymer layer of poly-PETA was obtained, as described in the previous section. For the second polymerization, the irradiation conditions used were 35 mW/cm^2 for 600 s in the presence of HFBA (Fig. 5eiii and fiii). We observe a thicker polymer layer and conclude that repolymerization from the first polymer is possible with a fluorinated monomer (HFBA, Fig. 5g), as schematically depicted in Fig. 5h. A copolymer is created since the development step performed after irradiation would easily remove the second polymer layer if no covalent bound was created. Interestingly, we noticed that the second polymerization was less efficient than that for TMPTA, as revealed by a thinner polymer layer. A possible reason may be the higher diffusion rate of the oxygen in the low-viscosity fluorinated monomer. Inhibition by oxygen may thus be more pronounced under these conditions [58].

Conclusions

We have demonstrated that PhotoATRP can be triggered by plasmon resonance excitation to generate multilayer covalent polymer parts with spatial control at the nanoscale. From a fundamental point of view this shows that PhotoATRP systems can be used with nanometer-scale spatial resolution. Despite the very limited number of photoactivable molecules embedded in the polymer shell, these species are accessible for further reaction and still reactivable to graft a second layer. This route provides a new degree of freedom for the fine tuning of the geometry and surface chemistry of nanoobjects, with the unique feature to realize this in a nonisotropic way. It also shows that fine surface functionalization of metal nanostructures can be realized with very precise control over the spatial distribution of the functional material. The achievements described in this work thus represent a major milestone in the development of advanced functional hybrid nanoparticles.

CRediT authorship contribution statement

Farid Kameche: Investigation, Methodology, Formal analysis, Visualization, Writing - original draft, Writing - review & editing.

Please cite this article in press as: F. Kameche et al., Materials Today (2020), https://doi.org/10.1016/j.mattod.2020.03.023

Wajdi Heni: Investigation, Methodology. **Siham Telitel:** Investigation, Methodology. **Dandan Ge:** Resources, Software. **Loïc Vidal:** Resources. **Fréderic Dumur:** Resources, Writing - review & editing. **Didier Gigmes:** Writing - review & editing. **Jacques Lalevée:** Writing - review & editing. **Sylvie Marguet:** Resources, Writing - review & editing. **Ludovic Douillard:** Resources, Software, Writing - review & editing. **Céline Fiorini-Debuisschert:** Writing - review & editing. **Renaud Bachelot:** Conceptualization, Writing - review & editing. **Olivier Soppera:** Conceptualization, Methodology, Visualization, Writing - original draft, Writing - review & editing, Supervision.

Acknowledgements

The authors gratefully thank the funding agency Agence Française pour la Recherche (ANR) for their financial support of this project under grants IMPACT: ANR2011BS08016, HAPPLE: ANR-12-BS10-016 and SAMIRE: ANR-13-NANO-0002.

Data availability

The raw/processed data required to reproduce these findings cannot be shared at this time due to technical limitations.

Appendix A. Supplementary data

Supplementary data to this article can be found online at https://doi.org/10.1016/j.mattod.2020.03.023.

References

[1] J. Nicolas et al., Prog. Polym. Sci. 38 (2013) 63–235.
[2] X.G. Qiao et al., Macromolecules 50 (2017) 3796–3806.
[3] J. Morris et al., Polym. Chem. 6 (2015) 754–763.
[4] M. Zamfir et al., J. Mater. Chem. B 1 (2013) 6027.
[5] B. Cabannes-Boué et al., Polym. Chem. 8 (2017) 1760–1770.
[6] Q. Yang, J. Lalevée, J. Poly, Macromolecules 49 (2016) 7653–7666.
[7] H. Xing et al., RSC Adv. 6 (2016) 66444–66450.
[8] X. Pan et al., Macromolecules 48 (2015) 6948–6954.
[9] F. Nzulu et al., Polym. Chem. 6 (2015) 4605–4611.
[10] Y. Yagci et al., Visible light-induced atom transfer radical polymerization for macromolecular syntheses, in: K. Matyjaszewski, B.S. Sumerlin, N.V. Tsarevsky, J. Chiefari (Eds.), Controlled Radical Polymerization: Mechanisms, American Chemical Society, 2015, pp. 145–158.
[11] X. Liu et al., Polym. Chem. 9 (2018) 584–592.
[12] M. Chen, M. Zhong, J.A. Johnson, Chem. Rev. 116 (2016) 10167–10211.
[13] X. Pan et al., Prog. Polym. Sci. 62 (2016) 73–125.
[14] S. Dadashi-Silab, S. Doran, Y. Yagci, Chem. Rev. 116 (2016) 10212–10275.
[15] N. Corrigan et al., Chem. Soc. Rev. 45 (2016) 6165–6212.
[16] N. Zivic et al., ChemCatChem 8 (2016) 1617–1631.
[17] Q. Yang et al., Macromolecules 48 (2015) 1972–1980.
[18] Y. Guillaneuf et al., Macromol. Rapid Commun. 31 (2010) 1909–1913.
[19] S. Telitel et al., Adv. Mater. Interfaces 1 (2014) 140067.
[20] J. Laun et al., Chem. Commun. 54 (2018) 751–754.
[21] M. Bouzrati-Zerelli et al., New J. Chem. 42 (2018) 8261–8270.
[22] G. Raffy et al., Nanoscale 9 (2017) 16908–16914.
[23] G. Zhang et al., Macromolecules 44 (2011) 7594–7599.
[24] S. Telitel et al., J. Polym. Sci. Part Polym. Chem. 54 (2016) 702–713.
[25] Y. Zhao et al., Chem. Sci. 6 (2015) 2979–2988.
[26] M. Ciftci, Y. Yagci, Macromol. Rapid Commun. 39 (2018) 1800464.
[27] J. Lalevée et al., Beilstein J. Org. Chem. 10 (2014) 863–876.
[28] S. Telitel et al., Polym. Chem. 6 (2015) 613–624.
[29] M.-A. Tehfe et al., Macromol. Chem. Phys. 218 (2017) 1700192.
[30] K.M. Burridge et al., Macromol. Rapid Commun. 39 (2018) 1800093.
[31] B.P. Fors, C.J. Hawker, Angew. Chem. Int. Ed. 51 (2012) 8850–8853.
[32] C.W. Pester et al., J. Polym. Sci. Part Polym. Chem. 54 (2016) 253–262.
[33] C.-G. Wang et al., Angew. Chem. 130 (2018) 13692–13696.
[34] H. Ibn El Ahrach et al., Phys. Rev. Lett. 98 (2007) 107402.
[35] H. Ibn-El-Ahrach et al., J. Microsc. 229 (2008) 421–427.
[36] C. Deeb et al., ACS Nano 4 (2010) 4579–4586.
[37] C. Deeb et al., J. Am. Chem. Soc. 133 (2011) 10535–10542.
[38] C. Gruber et al., Appl. Phys. Lett. 106 (2015) 081101.
[39] K. Ueno et al., J. Am. Chem. Soc. 130 (2008) 6928–6929.
[40] N. Tian et al., Eur. J. Inorg. Chem. 2010 (2010) 4875–4885.
[41] C. Deeb et al., J. Phys. Chem. C 116 (2012) 24734–24740.
[42] M. Haggui et al., ACS Nano 6 (2012) 1299–1307.
[43] J. Rodríguez-Fernández et al., J. Phys. Chem. B 109 (2005) 14257–14261.
[44] Q. Ruan et al., Adv. Opt. Mater. 2 (2014) 65–73.
[45] U. Hohenester, A. Trügler, Comput. Phys. Commun. 183 (2012) 370–381.
[46] J. Waxenegger, A. Trügler, U. Hohenester, Comput. Phys. Commun. 193 (2015) 138–150.
[47] U. Hohenester, A. Trügler, IEEE J. Sel. Top. Quantum Electron. 14 (2008) 1430.
[48] [61] F.J. Garcia de Abajo, A. Howie, Phys. Rev. B 65 (2002) 115418; [62] F.J. Garcia de Abajo, Rev. Mod. Phys. 82 (209) (2010).
[49] P.B. Johnson, R.W. Christy, Phys. Rev. B 6 (1972) 4370–4379.
[50] K. Luke et al., Opt. Lett. 40 (2015) 4823–4826.
[51] S. Telitel et al., C. R. Chim. 19 (2016) 71–78.
[52] C. Croutxé-Barghorn et al., Adv. Mater. Opt. Electron. 10 (2000) 25–38.
[53] O. Soppera, S. Jradi, D.J. Lougnot, J. Polym. Sci. Part Polym. Chem. 46 (2008) 3783–3794.
[54] T. Ding et al., ACS Photon. 4 (2017) 1453–1458.
[55] Y. Wang et al., Nano Res. 11 (2018) 6384–6390.
[56] Y.H. Lee et al., COSMOS 06 (2010) 167–195.
[57] P. Nordlander et al., Nano Lett. 4 (2004) 899–903.
[58] Y. Amao, Microchim. Acta 143 (2003) 1–12.

Please cite this article in press as: F. Kameche et al., Materials Today (2020), https://doi.org/10.1016/j.mattod.2020.03.023